nature astronomy

Article

https://doi.org/10.1038/s41550-023-02172-w

Accretion of the earliest inner Solar System planetesimals beyond the water snowline

Received: 26 April 2023

Accepted: 24 November 2023

Published online: 9 January 2024

Check for updates

Damanveer S. Grewal [1,2,3,4] ✉, **Nicole X. Nie** [4,5], **Bidong Zhang** [6], **Andre Izidoro** [7] & **Paul D. Asimow** [4]

How and where the first generation of inner Solar System planetesimals formed remains poorly understood. Potential formation regions are the silicate condensation line and water snowline of the solar protoplanetary disk. Whether the chemical compositions of these planetesimals align with accretion at the silicate condensation line (water-free and reduced) or water snowline (water-bearing and oxidized) is, however, unknown. Here we use the Fe/Ni and Fe/Co ratios of magmatic iron meteorites to quantify the oxidation states of the earliest planetesimals associated with non-carbonaceous (NC) and carbonaceous (CC) reservoirs, representing the inner and outer Solar System, respectively. Our results show that the earliest NC planetesimals contained substantial amounts of oxidized Fe in their mantles (3–19 wt% FeO). In turn, we argue that this required the accretion of water-bearing materials into these NC planetesimals. The presence of substantial quantities of moderately and highly volatile elements in their parent cores is also inconsistent with their accretion at the silicate condensation line and favours, instead, their formation at or beyond the water snowline. Similar oxidation states in the early formed parent bodies of NC iron meteorites and those of NC achondrites and chondrites with diverse accretion ages suggest that the formation of oxidized planetesimals from water-bearing materials was widespread in the early history of the inner Solar System.

Chronological constraints on meteorites, in particular, magmatic iron meteorites (sampling the metallic cores of the first generation of planetesimals[1,2]), suggest that planetesimals began forming almost at the onset of Solar System formation[3,4]. Planetesimal formation is expected at locations of the disk where small solid particles (millimetre-to-centimetre sized pebbles) pile up to sufficient density to collapse under their collective gravity[5,6]. Pebbles are likely to pile up more efficiently in specific regions of the disk—the so-called snowlines—associated with the condensation/sublimation fronts of silicates, water and carbon monoxide[7–10]. Although there is a growing consensus that planetesimals associated with the carbonaceous (CC) reservoir (sampling the outer Solar System) formed at or beyond the water snowline[7–10], the formation zone of the first generation of non-carbonaceous (NC) planetesimals (sampling the inner Solar System) is poorly understood. Understanding the formation of the first NC planetesimals is of utmost importance because Earth and other terrestrial planets chiefly grew from such planetesimals[11,12].

Two competing models have been proposed to explain the formation of the first NC planetesimals. The first is that the formation of NC planetesimals was triggered at the water snowline during an early phase as the water snowline migrated out during disk infall (Class I stage), whereas CC planetesimals formed later at the water snowline

---

[1]School of Molecular Sciences, Arizona State University, Tempe, AZ, USA. [2]School of Earth and Space Exploration, Arizona State University, Tempe, AZ, USA. [3]Facility for Open Research in a Compressed Environment (FORCE), Arizona State University, Tempe, AZ, USA. [4]Division of Geological and Planetary Sciences, California Institute of Technology, Pasadena, CA, USA. [5]Department of Earth, Atmospheric, and Planetary Sciences, Massachusetts Institute of Technology, Cambridge, MA, USA. [6]Department of Earth and Space Sciences, University of California, Los Angeles, CA, USA. [7]Department of Earth, Environmental and Planetary Sciences, Rice University, Houston, TX, USA. ✉e-mail: damanveer.grewal@asu.edu

as it migrated back in during subsequent evolution of the disk (Class II stage)[7,8]. The alternative view is that NC and CC planetesimals formed contemporaneously at the silicate condensation line and water snowline, respectively[9,10]. At face value, the latter model is more appealing because magmatic NC irons, based on their chemical compositions, seem to be more reduced than their CC counterparts[4,13,14]. Formation of NC iron meteorite parent bodies (IMPBs) at the silicate condensation line should have resulted in their accreting water-free materials, whereas CC IMPBs forming at the water snowline should have accreted water-rich materials[9,10]. As water was the primary oxidizing agent in the early forming planetesimals[15–17], accretion of NC and CC IMPBs at the silicate condensation line and water snowline, respectively, can qualitatively account for their contrasting oxidation states[4]. Accretion of substantial amounts of ice by CC IMPBs is also postulated to delay their onset of melting (by lowering the concentration of heat producing ^{26}Al) and subsequent core formation, relative to the anhydrous NC IMPBs[4]. Therefore, even though the radiometric dating-derived core formation ages of CC IMPBs are ~2 million years younger than their NC counterparts[1,3], they could have accreted almost contemporaneously[4]. In short, accretion of NC and CC IMPBs at the silicate condensation line and water snowline, respectively, is an appealing hypothesis given that it appears to be simultaneously consistent with their distinct oxidation states and, potentially, contemporaneous accretion ages. However, whether the differences in chemical characteristics, in particular, oxidation states, of NC and CC IMPBs are truly consistent with their accretion at the silicate condensation line and water snowline, respectively, remains elusive because their oxidation states and associated water contents have not been constrained quantitatively. Therefore, whether the first inner Solar System planetesimals formed at the silicate condensation line, and thereby accreted reduced and dry materials, needs to be tested.

Here we calculate the oxygen fugacity (fO_2) of core–mantle differentiation in magmatic NC and CC IMPBs to constrain the oxidation states of the first generation of planetesimals in each reservoir. Metal–silicate equilibration in partially to fully molten planetesimals established the chemical compositions of the parent cores of magmatic irons[13,18]. At the relatively low pressure and temperatures applicable for core–mantle differentiation in IMPBs, elemental exchange between the metallic cores and silicate mantles is controlled by the fO_2 of metal–silicate equilibration ($\mathrm{M_{(metal)}} + n/2\ \mathrm{O_{2(g)}} = \mathrm{MO}_{n/2\mathrm{(silicate)}}$) (ref. 18). Hence, the oxidation states of bulk planetesimals can be determined as long as the compositions of their cores and mantles are known. The bulk compositions of the parent cores of magmatic irons can be reconstructed by integrating fractional crystallization models and elemental abundances in iron meteorites[13,19–22]. However, the lack of coexisting silicate compositions for magmatic irons presents the principal challenge in constraining the oxidation states of their parent bodies. An alternative approach to constrain the oxidation states of bulk planetesimals during core–mantle differentiation is through the relative depletion of elements in the parent cores that possess similar volatilities but varying degrees of siderophile (metal-loving) character[18]. Fe, Co and Ni have similar volatilities[23] and hence do not fractionate during condensation and/or evaporation processes. By contrast, Fe (major element in the cores) can be fractionated relative to Co and Ni at fO_2 relevant for core–mantle differentiation because of its less siderophile character ($D_{\mathrm{Fe}}^{\mathrm{metal/silicate}}$ (concentration of Fe in metal/concentration of Fe in silicate) ≈ 1–10 versus $D_{\mathrm{Ni\ or\ Co}}^{\mathrm{metal/silicate}} \approx 100$–3,000) (ref. 24). This is linked to the positions of the Co–CoO and Ni–NiO buffers, which are ~2 and 4 log units higher in fO_2, respectively, than the iron-wüstite (IW) buffer (the maximum fO_2 to form substantial Fe-rich cores in rocky bodies), at temperatures relevant for core–mantle differentiation[18]. The depletion of Fe relative to Ni and Co in the cores can directly constrain the amount of oxidized Fe in the mantles and, as a result, the fO_2 of bulk planetesimals relative to the IW buffer.

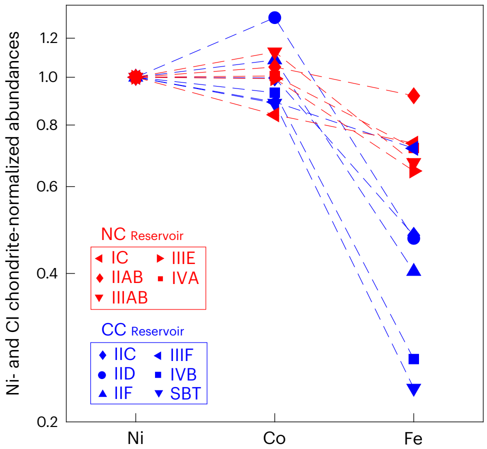

Fig. 1 | Ni and CI-chondrite normalized bulk Ni, Co and Fe contents in the parent cores of magmatic iron meteorites. $(\mathrm{Co/Ni})_{\mathrm{CI}}$ ratios of NC and CC irons are close to 1 (except for group IID) and do not show any systematic differences between NC and CC irons. $(\mathrm{Fe/Ni})_{\mathrm{CI}}$ ratios of both NC and CC irons are both lower than 1, with CC irons (except for group IIIF) having systematically lower $(\mathrm{Fe/Ni})_{\mathrm{CI}}$ ratios than NC irons. NC and CC iron meteorites are shown in red and blue, respectively.

Results

Fractional crystallization models have been previously combined with iron meteorite data to estimate the concentrations of Fe, Ni and Co in the majority of iron meteorite parent cores (Extended Data Table 1)[13,19–22]. We applied a similar model to calculate the currently unknown $C_{\mathrm{Ni}}^{\mathrm{core}}$ and $C_{\mathrm{Fe}}^{\mathrm{core}}$ of group IIIE and $C_{\mathrm{Co}}^{\mathrm{core}}$ of IC, IIAB and IIIE cores, where C is the concentration of an element in a reservoir (Extended Data Fig. 1 and Extended Data Table 1; see Methods for details). The $(\mathrm{Co/Ni})_{\mathrm{CI}}$ ratios (that is, the Co/Ni ratio normalized to the ratio in CI chondrites) of the parent cores of both NC and CC irons (except for group IID) are close to 1 (Fig. 1). There are no systematic differences between the $(\mathrm{Co/Ni})_{\mathrm{CI}}$ ratios of NC and CC irons. This suggests that there was limited fractionation between Co and Ni during core–mantle differentiation in both NC and CC IMPBs, irrespective of the variation in their oxidation states. The limited fractionation can be readily explained if Co and Ni, in agreement with their high metal–silicate partition coefficients at low pressures[18], almost exclusively partitioned into the cores of both NC and CC IMPBs. This implies near-quantitative reduction of all Co and Ni into the cores without fractionation between them during core–mantle differentiation. $(\mathrm{Fe/Ni})_{\mathrm{CI}}$ ratios of the parent cores of both NC and CC irons are, however, lower than 1 (Fig. 1). As reported in previous studies[4,13], CC cores generally have lower $(\mathrm{Fe/Ni})_{\mathrm{CI}}$ ratios than NC cores, except for the CC group IIIF, which overlaps the NC groups. Lower Fe contents in the CC cores are a result of a higher retention of Fe as FeO in the mantles of their parent bodies during core–mantle differentiation, which implies that CC IMPBs were more oxidized than their NC counterparts[4]. This observation also agrees with the relative enrichment of highly siderophile elements and, consequently, smaller core/mantle mass ratios, in CC IMPBs relative to NC IMPBs[13].

Establishing the oxidation states of NC and CC IMPBs (as fO_2 relative to the IW buffer) requires constraints on the amount of oxidized Fe retained in their mantles during core–mantle differentiation. Because the bulk Fe contents of the IMPBs are unknown, a direct mass balance of Fe between mantles and cores cannot be used for this exercise. The bulk Fe/Ni and Fe/Co ratios of chondrites, however, show limited variations across all groups of NC and CC chondrites (standard deviations divided by the means are less than 4%)[25]. As the chondritic Fe/Ni and Fe/Co ratios are also similar to solar values[26], it is reasonable to assume that the earlier forming NC and CC IMPBs also had chondritic Fe/Ni and Fe/Co ratios. Therefore, the mass balance of Fe between mantles and

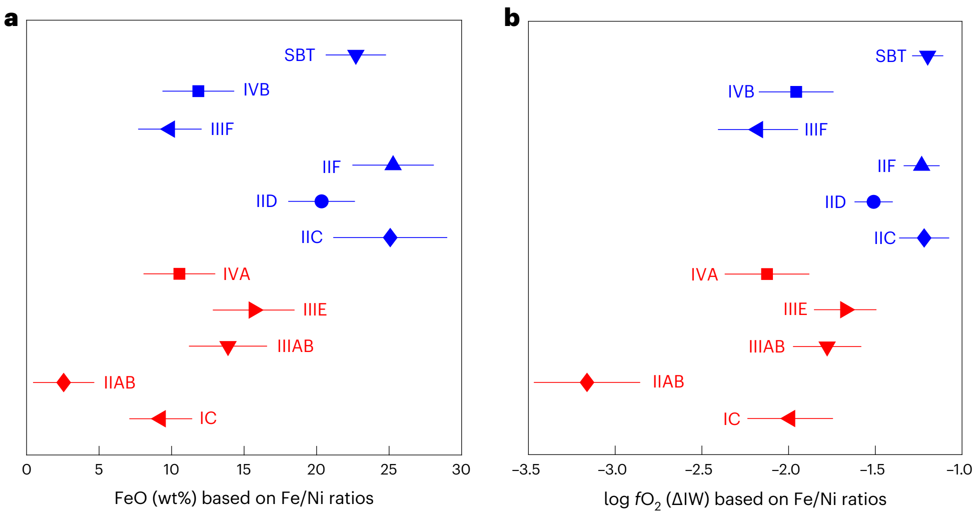

Fig. 2 | Comparison between the FeO contents and fO_2 of IMPBs based on the Fe/Ni ratios of their parent cores. a,**b**, The FeO contents (**a**) and fO_2 (**b**) of CC IMPBs (blue), except for groups IIIF and IVB, are only modestly higher than those of NC IMPBs (red). Error bars for FeO content and fO_2 represent 1*σ* from the mean obtained by the propagation of standard deviation of individual terms in equations (1) and (2), respectively. Uncertainties in the compositions of the parent cores of iron meteorites are not reported in the literature[13,19–21]. Therefore, to determine 1*σ* uncertainties, we assigned a conservative 5% uncertainty to each of the concentrations of Fe, Ni and Co in the cores and bulk Fe/Ni and Fe/Co ratios in CI chondrites. For the core/mantle mass ratio, we used the uncertainties reported in ref. 13.

cores in tandem with those of Ni and Co (assuming that all Ni and Co partition into the cores) can be used to quantify the Fe contents of the mantles of IMPBs by using the equation

$$C_{\mathrm{Fe}}^{\mathrm{mantle}} = \left[\left(\frac{\mathrm{Fe}}{\mathrm{Ni\ or\ Co}}\right)^{\mathrm{bulk}} \times C_{\mathrm{Ni\ or\ Co}}^{\mathrm{core}} - C_{\mathrm{Fe}}^{\mathrm{core}}\right] \times r \qquad (1)$$

where *r* is the core/mantle mass ratio. Core/mantle mass ratios for NC and CC IMPBs were established previously based on the enrichment of highly siderophile elements in their parent cores relative to chondrites[13]. $\left(\frac{\mathrm{Fe}}{\mathrm{Ni}}\right)^{\mathrm{bulk}}$ and $\left(\frac{\mathrm{Fe}}{\mathrm{Co}}\right)^{\mathrm{bulk}}$ ratios of both NC and CC IMPBs were assumed to have CI chondrite-like values (17 and 357, respectively)[25]. With these constraints, the FeO contents of the mantles (assuming that all oxidized Fe is FeO) of NC IMPBs computed from Fe/Ni lie in the range 3–16 wt% and those based on Fe/Co are 4–19 wt% (Fig. 2a, Extended Data Fig. 2a and Extended Data Table 2). Likewise, the FeO contents of the mantles of CC IMPBs computed from Fe/Ni are 10–25 wt% and those based on Fe/Co are 6–33 wt% (Fig. 2a and Extended Data Fig. 2a). Hence, the FeO contents of CC IMPBs are generally higher than those of their NC counterparts (except for the overlap of groups IIIF and IVB with NC IMPBs), but the overall differences are small. Lower Fe/Ni and Fe/Co in CC irons are partially offset by their lower core/mantle mass ratios, which leads to less pronounced differences in the FeO contents of NC and CC IMPBs (equation (1)). The calculations from Fe/Ni and from Fe/Co are broadly in agreement (Extended Data Fig. 3a), except for groups IC and IID. The source of the discrepancy for these two groups is unknown; it is potentially related to uncertainties in the fractional crystallization models used to estimate the Ni and Co contents of the parent cores or to variations from the CI ratio in the Ni/Co ratios of their parent bodies. Given the limited range in Fe/Ni and Fe/Co ratios across all groups of chondrites[25], our results are not sensitive to the choice of chondrite group used to represent the bulk Fe/Ni and Fe/Co ratios of IMPBs. For example, our results are virtually identical if Fe/Ni and Fe/Co ratios of ordinary chondrites (OCs) or CM chondrites are assumed for NC and CC IMPBs, respectively, in place of CI chondrites in equation (1) (Extended Data Fig. 4).

The oxidation states of rocky bodies—represented as fO_2 relative to the IW buffer (governed by the reaction $\mathrm{Fe}^{\mathrm{metal}} + 1/2\,\mathrm{O}_2 = \mathrm{FeO}^{\mathrm{silicate}}$)—can be estimated using the equation

$$\log fO_2(\Delta\mathrm{IW}) = 2\log\frac{a_{\mathrm{FeO}}^{\mathrm{silicate}}}{a_{\mathrm{Fe}}^{\mathrm{metal}}} = 2\log\frac{X_{\mathrm{FeO}}^{\mathrm{silicate}} \times \gamma_{\mathrm{FeO}}^{\mathrm{silicate}}}{X_{\mathrm{Fe}}^{\mathrm{metal}} \times \gamma_{\mathrm{Fe}}^{\mathrm{metal}}} \qquad (2)$$

where $a_{\mathrm{FeO}}^{\mathrm{silicate}}$, $X_{\mathrm{FeO}}^{\mathrm{silicate}}$ and $\gamma_{\mathrm{FeO}}^{\mathrm{silicate}}$ are the activity, mole fraction and activity coefficient of FeO component in the silicates and $a_{\mathrm{Fe}}^{\mathrm{metal}}$, $X_{\mathrm{Fe}}^{\mathrm{metal}}$ and $\gamma_{\mathrm{Fe}}^{\mathrm{metal}}$ are the activity, mole fraction and activity coefficient of the Fe component in the metals[18]. We estimated the fO_2 values of IMPBs by means of the ideal solution model ($\gamma_{\mathrm{Fe}}^{\mathrm{metal}}$ and $\gamma_{\mathrm{FeO}}^{\mathrm{silicate}} = 1$) to compare our results with the previous reports of fO_2 in chondrites, achondrites and rocky planets (Extended Data Table 2). The range of fO_2 of metal–silicate equilibration in NC IMPBs implied by Fe/Ni is IW −3.2 to IW −1.7, whereas Fe/Co gives IW −2.8 to IW −1.5 (Fig. 2b, Fig. 3 and Extended Data Fig. 2b). By contrast, the range of fO_2 of metal–silicate equilibration in CC IMPBs based on Fe/Ni is IW −2.2 to IW −1.2 and based on Fe/Co it is IW −2.6 to IW −1.1 (Figs. 2b and 3 and Extended Data Fig. 2b). Although CC IMPBs are modestly more oxidized than NC IMPBs, the fO_2 of groups IIIF and IVB overlap with their NC counterparts. Note that higher S contents in the parent cores of NC IMPBs[13] result in lower $X_{\mathrm{Fe}}^{\mathrm{metal}}$, which partially offsets the differences between fO_2 of NC and CC IMPBs. Just as the mantle FeO contents for each NC and CC IMPB based on Fe/Ni and Fe/Co are similar, the estimates of fO_2 of metal–silicate equilibration implied from these two ratios are broadly in agreement (variations less than 0.8 log units), except for groups IC and IID (Extended Data Fig. 3b). Although fractional crystallization models yield non-unique solutions to the initial compositions of the parent cores, the calculated FeO content and fO_2 of each IMPB remain consistent within the range of initial Fe, Ni and Co contents predicted by previous studies[13,19–22] (Extended Data Fig. 5).

We also extended our findings to a set of ungrouped irons that are presumed to be magmatic (based on their fractionated Ir/Au ratios)[27] and whose heritage from the NC or CC reservoirs has been established previously[28] (Fig. 3 and Extended Data Table 3; see Methods for details). Although the bulk compositions of the ungrouped magmatic irons are not as well characterized as those of the grouped magmatic irons, the fO_2 of core–mantle differentiation in the ungrouped IMPBs from the NC reservoir is not drastically different from the ungrouped and grouped CC IMPBs (Fig. 3). Combined, the major conclusion of this exercise

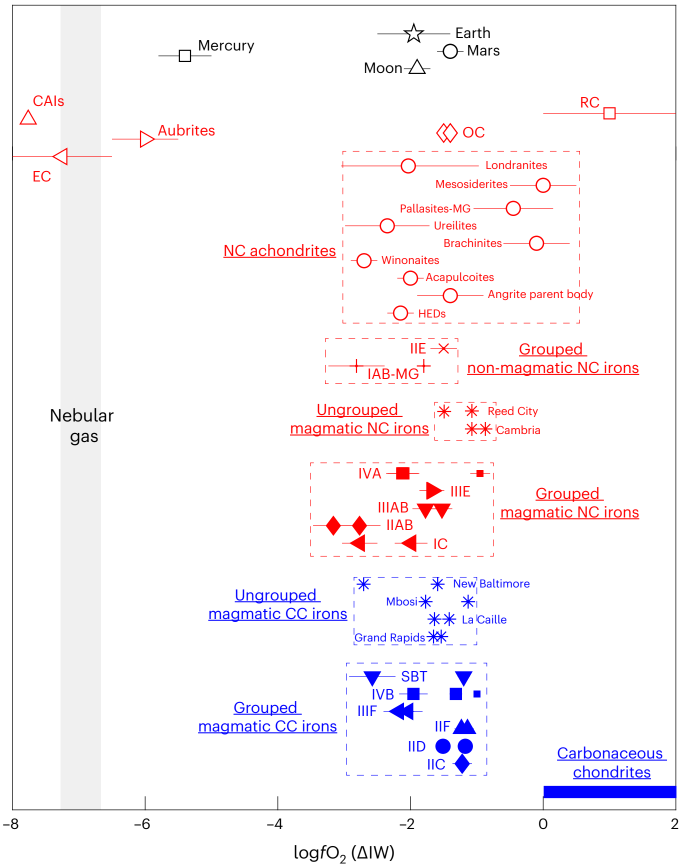

Fig. 3 | Variations in the oxidation states of various Solar System objects and reservoirs. The fO_2 of all rocky bodies in the NC (red) and CC (blue) reservoirs (except for the EC and aubrite parent bodies) are several orders of magnitude higher than the nebular gas and CAIs[47]. Grouped NC IMPBs are not drastically more reduced than their CC counterparts. The fO_2 of grouped NC IMPBs are similar to those of ungrouped IMPBs, non-magmatic irons, OCs and several other groups of achondrites from the NC reservoir. The fO_2 prevailing during core–mantle differentiation of Earth (final event), Mars and the Moon also lie within the range of grouped NC IMPBs and other oxidized NC planetesimals. The two symbols for each grouped and ungrouped magmatic iron represent fO_2 calculated using their Fe/Ni and Fe/Co ratios. The smaller symbols for IVA and IVB groups represent fO_2 estimates from previous studies[18,29]. Error bars for grouped and ungrouped magmatic irons represent 1σ deviation from the mean obtained by the propagation of uncertainty from individual terms in the fO_2 calculation of equation (2). The plotted data are reported in Extended Data Tables 2–4.

is that there are only modest differences between the fO_2 prevailing during core–mantle differentiation in NC and CC IMPBs.

Discussion

Oxygen fugacity of the NC parent bodies

Our estimates for fO_2 of magmatic NC IMPBs are comparable with previous estimates for some of these bodies (for example, IW −1.0 for group IVB (ref. 18) and IW −0.95 for group IVA (ref. 29)) (Fig. 3 and Extended Data Table 4). These estimates are also similar to the fO_2 of non-magmatic NC iron groups determined by mineral equilibria between the coexisting metals and silicates (for example, IW −2.8 to IW −1.8 for group IAB-MG (refs. 30,31) and IW −1.5 for group IIE (ref. 31)). The fO_2 of several other primitive and asteroidal NC achondrites are also comparable with our constraints for NC IMPBs. For example, HEDs yield IW −2.2 (refs. 24,32); angrites IW −1.4 (refs. 24,32); acapulcoites IW −2.0 (refs. 30,31); winonaites IW −2.7 (refs. 30,31); brachinites IW −0.6 to IW + 0.4 (ref. 33); pallasites-MG IW −1.1 to IW + 0.9 (ref. 33); lodranites IW −3.1 to IW − 0.9 (ref. 33); ureilites IW −2.4 (ref. 34); and mesosiderites IW −0.5 to IW + 0.5 (ref. 35) (Fig. 3 and Extended Data Table 4). These values are also comparable with the estimated fO_2 of OCs (between IW −2.2 and IW −1.5) (refs. 31,36) whereas Rumuruti chondrites record an even more oxidized alteration environment (IW to IW +2) (refs. 33,37).

All these NC planetesimals, including NC IMPBs, record distinctly higher fO_2 than the two groups of extremely reduced NC meteorites, enstatite chondrites (ECs) (IW −8.0 to IW −6.5 (ref. 38)) and aubrites (IW −6.5 to IW −5.5 (refs. 39,40)) (Fig. 3). The Si contents of NC iron meteorites provide further strong evidence that their parent bodies did not accrete from extremely reduced materials akin to ECs and aubrites. Si becomes siderophile during metal–silicate equilibration under extremely reduced conditions, such that the cores of planetesimals accreting EC- and aubrite-like materials (containing up to 3 wt% Si in the metal[41,42]) must contain several wt% Si (up to 20 wt%)[39]. However, Si-bearing iron meteorites are extremely rare; >99% of iron meteorites contain <30 ppm Si in the metal[43,44]. The combined evidence suggests that the oxidation states of NC IMPBs were not drastically different from those of CC IMPBs. The similarity of the oxidation states of NC IMPBs with almost all meteorites from the NC reservoir (except ECs and aubrites), covering a wide range of accretion ages (~0.1–4 million years after the formation of calcium-aluminum-rich inclusions (CAIs)—the oldest solids which date 'time zero' in Solar System history)[4,45] suggests that the formation of oxidized NC planetesimals was the norm rather than the exception.

Consequences of oxidized NC parent bodies

High-temperature experiments and thermodynamic calculations predict that equilibrium fO_2 during the condensation of nebular solids in the NC reservoir, from a gas with a solar C/O ratio of ~0.5, was ~7 log units below the IW buffer[46,47] (Fig. 3). At such reduced conditions, Fe condenses as metallic Fe,Ni-alloy and the cocondensing silicates contain only trace amounts of FeO (ref. 46). Ti^{3+}/Ti^{4+} and FeO/(FeO + MgO) ratios in CAIs attest to equilibrium condensation of nebular solids under such extremely reduced conditions[47] (Fig. 3). In contrast, oxidized Fe is prevalent in the chondrules and matrices of ordinary and Rumuruti chondrites from the NC reservoir. For example, the olivine FeO contents in the type I chondrules of OCs can be up to 10 wt% and type II chondrules contain more than 10 wt% FeO (refs. 48,49). These high FeO contents cannot be explained by the evaporation and condensation of anhydrous, FeO-free dust in any known nebular environment[15]. Isotopic compositions of chondrules in ordinary and Rumuruti chondrites also rule out large-scale transport of FeO-bearing oxidized dust from the CC to the NC reservoir in the early Solar System[50]. Hence, the oxidized nature of early NC planetesimals implies the involvement of an external mechanism to increase fO_2 in systems that were otherwise solar in composition.

The first formation of substantial FeO has been linked to environments where the H_2O/H_2 ratio was much greater (~10^{-1}) than that of nebular gas (~10^{-4}) (refs. 15,17,51). Heating of dust in the protosolar nebula with locally enhanced dust/gas ratios is a viable pathway to producing silicates with substantial FeO contents only if the precursor dust was water-bearing—for example, a mixture of solar condensate dust and ice or structurally bound water in phyllosilicates[15,17,52]. An arguably simpler setting is the interaction of aqueous fluids, generated by the melting of ice during ^{26}Al decay, with metallic Fe within planetesimals that grew from ice-bearing materials[15,17]. This interaction can form substantial amounts of FeO by the well-characterized reaction, $Fe_{(s)} + H_2O_{(l)} = FeO_{(s)} + H_{2(g)}$ (ref. 15). The high porosity and permeability of planetesimals before high-temperature sintering allows the efficient escape of H_2 and the ensuing oxidation of the bulk planetesimals[53]. This scenario has also been suggested to explain the production of FeO-bearing chondrule precursors where liquid water interacted with metallic Fe and magnesium silicates at elevated temperatures within planetesimals[15,17].

There is ample evidence supporting a relationship between the presence of abundant oxidized Fe in chondrites (including ordinary and

Rumuruti chondrites from the NC reservoir) and a history of aqueous alteration[16,53]. Primitive members of some chondrite groups contain more metal in the matrix and chondrules than their aqueously altered counterparts[53,54]. Oxidation rinds of magnetite[16] surrounding Fe–Ni alloys have also been attributed to parent-body aqueous alteration. In fact, the sequence of increasing fO_2 among chondrite classes—from bulk ECs to OCs, Rumuruti chondrites and carbonaceous chondrites—positively correlates with the water contents and aqueous alteration signatures[55]. It is important to note that, in contrast to chondrites, whose water inventory can potentially be explained by the late addition of water-bearing materials to the surfaces of their parent bodies, the cores of IMPBs record the oxidation state of the entire planetesimals and cannot be a late alteration signature.

We calculated the water contents required to explain the FeO contents of IMPBs by means of aqueous alteration of anhydrous dust. Production of the entire FeO inventory of NC IMPBs by aqueous alteration requires ~1–5 wt% water equivalent (Extended Data Fig. 6). Note that this estimate is a minimum bound for the water/ice inventory accreted by NC IMPBs because such water can have several other fates apart from oxidizing Fe and being lost as H_2: water may have reacted with other anhydrous components (for example, matrix)[16] or percolated outwards as aqueous fluid without reacting with the rocky materials[7]. A substantial loss of water inventory during heating/differentiation has also been reported for differentiated CC planetesimals[56]. In comparison, the present H_2O/OH contents in ordinary and Rumuruti chondrites are in the range of ~1–4 wt% (ref. 55). However, the primitive water inventories of the parent bodies of ordinary and Rumuruti chondrites are also argued to be much higher than these estimates because of water loss during metamorphic dehydration and consumption of water during oxidation of Fe and other anhydrous components[53,55].

The oxidation states of NC IMPBs, therefore, are likely to record a water-enriched formation environment by means of the accretion of either ice or phyllosilicates. Different Solar System scenarios can potentially generate such environments. These include:

1. formation of NC IMPBs at the water snowline as it moved inwards, followed by the rapid formation of Jupiter's core[3] beyond the water snowline separating the NC and CC reservoirs;
2. the presence of a dynamic water snowline periodically drifting in and out in the solar protoplanetary disk due to variations in the infall accretion rate onto the Sun[57,58]. The transient passage of the water snowline through the inner part of the disk could have triggered the formation of ice-rich NC IMPBs; and
3. delivery of oxidized Fe and water by means of phyllosilicate-bearing dust/pebbles[59] to a pressure bump inside the water snowline where NC IMPBs could grow. However, the limited thermal stability of phyllosilicates (<800 K) (ref. 16) suggests that the silicate condensation line (with a condensation temperature of ~1,400 K) cannot be the location of that pressure bump. Pressure bumps associated with poorly understood processes such as long-lived zonal flows[60] could, however, explain the formation of NC IMPBs between the silicate sublimation line and water snowline where phyllosilicates are stable. However, the efficiency of phyllosilicate formation by means of nebular processes is currently debated and is generally considered to be a parent body process[16,17], which makes the water snowline a more plausible location for the formation of NC IMPBs.

Further implications

The presence of water-bearing conditions during the accretion of NC IMPBs raises doubts about the predicted contemporaneous accretion ages of NC and CC IMPBs. The ~2 million year difference in their core–mantle differentiation ages can only be explained if NC and CC IMPBs accreted ice-free and ice-bearing materials, respectively[4]. However, the findings of this study suggest that NC and CC IMPBs did not have drastically different oxidation states and ensuing water contents. These differences are not sufficient to account for the ~2 million year delay in the formation of the cores of CC IMPBs because a substantial difference in water contents (~20–30 wt%) between NC and CC IMPBs would be required for such an explaination[4]. Thus, the observed disparity in their core formation ages is likely to reflect the later accretion of CC IMPBs[3]. A delayed accretion of CC IMPBs would result in lower ^{26}Al content, thereby causing lesser dehydration and protracted hydrothermal activity[7] and, subsequently, greater oxidation of Fe in their bodies.

A water-bearing character for the building blocks of NC IMPBs does not require that they remained water-rich planetesimals after differentiation. ^{26}Al decay-powered heating would have resulted in large-scale dehydration of the earliest formed planetesimals[7,61]. As discussed previously, H_2O could be lost by outgassing of H_2 or by outflow of aqueous fluids. A similar mechanism has been postulated to explain the loss of other highly volatile elements (HVEs) such as nitrogen and carbon from these planetesimals[62,63]. Comparably low water contents of NC and CC achondrites also attest to efficient dehydration of planetesimals during differentiation[56]. Consequently, despite the case we have constructed for their elevated initial water contents, the contribution, if any, of these differentiated planetesimals to the water budget of Earth and other terrestrial planets may have been quite limited.

The presence of nitrogen and carbon in NC iron meteorites suggests that their parent bodies, in addition to water, accreted other HVEs[63–67]. Also, the parent cores of multiple groups of NC IMPBs contained several wt% S (up to 19 wt%)[13,68] and high amounts of moderately volatile elements (MVEs) such as germanium, gallium, arsenic, antimony and copper, with 50% condensation temperatures lower than 1,100 K (refs. 2,20). Had the NC IMPBs accreted at the silicate condensation line, their cores should have been almost free of siderophile HVEs and MVEs, which is not the case. Together with the evidence compiled here for the action of H_2O in producing FeO during or before core–mantle differentiation, the HVE and MVE data argue against formation of early NC planetesimals at the silicate condensation line. Only the EC and aubrite parent bodies plausibly formed in such a hot and reduced water-poor environment. Yet even the ECs contain substantial amounts of HVEs and MVEs in both high-temperature and low-temperature components (chondrules and matrix, respectively)[41], which casts doubts on their origin at the silicate condensation line.

The dichotomy between the oxidation states of the ECs and aubrites with those of magmatic irons, non-magmatic irons, ordinary and Rumuruti chondrites and several other NC achondrites suggests that there were two distinct mechanisms of planetesimal formation in the NC reservoir (Fig. 3). The parent bodies of extremely reduced and water-poor ECs and aubrites accreted in the innermost part of the NC reservoir where the water snowline never reached. All other NC meteorites sampling oxidized planetesimals are likely to have accreted at or beyond the water snowline. The spread in the accretion ages of oxidized NC meteorites (~0.1–4 million years after CAIs)[4,45,69] suggests that oxidized planetesimals formed continually in the NC reservoir right from the onset of Solar System formation, whereas only late accreting planetesimals (>1.5 million years after CAIs; based on the accretion ages of the EC and aubrite parent bodies)[45] are sampled from the reduced part of the NC reservoir. Did EC- and aubrite-like planetesimal formation start late or are early forming planetesimals from that reservoir missing in the meteorite record? Answering this question is critical to understanding the oxidation states and chemical compositions of the seeds of rocky planets such as Earth and Mars, which primarily grew from NC planetesimals[11,12,70].

Methods

Fractional crystallization models

Bulk Fe, Ni and Co concentrations in the parent cores of groups IIC, IID, IIF, IVB and SBT are compiled from ref. 19, group IIIF from ref. 22, group IIIAB from ref. 20 and group IVA from ref. 21 (Extended Data Table 1). Bulk Fe and Ni concentrations of groups IC and IIAB cores are compiled from ref. 13. Bulk Co concentrations of IC and IIAB cores are calculated by means of fractional crystallization models by using the bulk S concentrations of ref. 13 and the lowest Co concentrations (assumed to sample the first crystallized solids) from IC and IIAB groups[71,72]. Bulk S, P, Co and Ni concentrations are acquired by the fractional crystallization modelling of P-Ni, Ir-Co and Ir-Ni trends for group IIIE (Extended Data Fig. 1). Ir, Co and Ni data of IIIE irons are from ref. 73 and P data is from ref. 74.

The methods used for fractional crystallization modelling are described in the literature[20,68]. Here is a short summary. The modelling uses batch crystallization in small steps to simulate fractional crystallization of metallic melts. In metallic melts, the partition coefficients of trace elements change as the liquid composition (in particular, their S and P concentrations) changes during crystallization. The remaining liquid of a step is used as the starting liquid of the next step.

The equilibrium batch crystallization is a simple mass balance between the phase fields,

$$\frac{C_\mathrm{L}}{C_\mathrm{i}} = \frac{1}{(1 - f + f \times D_\mathrm{E})} \tag{3}$$

In equation (3), C_i, C_L, f and D_E represent the bulk composition of the liquid, the bulk composition of the remaining liquid, the crystallization step and the partition coefficient of an element between solid and liquid metal, respectively. The models in this study used a constant of 0.001 for each mass step. The concentration of an element in the solid (C_s), which is derived from each mass step, is calculated using the bulk composition of the remaining liquid and the partition coefficient of the element in that step,

$$C_\mathrm{s} = D_\mathrm{E} \times C_\mathrm{L} \tag{4}$$

The partition coefficient of an element is strongly influenced by the S and P contents of the liquid and varies at each small step. D_E is parameterized using equation (5) as

$$D_\mathrm{E} = D_0 \times (Fe\ domains)^{\beta} \tag{5}$$

where D_0 is the partition coefficient of an element in the S- and P-free system, β is a constant specific to an element related to S and P in the liquid and *Fe domains* represent the fraction of free Fe atoms available in the liquid[68]. *Fe domains* in the Fe–Ni–S–P system were calculated by equation (6) and $\beta_{\mathrm{S+P}}$ of an element in the Fe Ni S P system was calculated using equation (7) from ref. 75.

$$Fe\ domains = \frac{1 - 2X_\mathrm{S} - 4X_\mathrm{P}}{1 - X_\mathrm{S} - 3X_\mathrm{P}} \tag{6}$$

$$\beta_{\mathrm{S+P}} = \left[\frac{2X_\mathrm{S}}{(2X_\mathrm{S} + 4X_\mathrm{P})}\right]\beta_\mathrm{S} + \left[\frac{4X_\mathrm{P}}{(2X_\mathrm{S} + 4X_\mathrm{P})}\right]\beta_\mathrm{P} \tag{7}$$

where X_S and X_P are the molar fractions of S and P in the liquid, respectively. β_S and β_P are the beta values for each element in the Fe–S and Fe–P systems, respectively.

The scattered interelement trends of group IIIE can be caused by the equilibrium mixing of solid and liquid (trapped melt)[76]. A recently revised version of the trapped-melt model considers the formation of troilite in the trapped melt[20]. The relationship between the trapped melt ($C_{\text{trapped melt}}$) and the solid ($C_{\text{trapped melt solid}}$) that crystallized from the trapped melt can be expressed using equation (8),

$$C_{\text{trapped melt solid}} = \frac{C_{\text{trapped melt}}}{1 - x} \tag{8}$$

where x denotes the mass fraction of the trapped melt that solidifies to form troilite.

Ungrouped irons do not belong to any existing iron meteorite groups and they are either from magmatic cores or non-magmatic impact-melt pools[2,77]. The latter did not go through fractional crystallization. Among the target ungrouped irons, Cambria, Reed City, Grand Rapids, La Caille, Mbosi and New Baltimore are likely to have had magmatic origins[77]. We used fractional crystallization models to estimate the bulk compositions of their parent cores. Although these estimates are not as accurate as those for grouped iron meteorites, they can still yield useful points of comparison. Due to the low variation of Ni and Co concentrations within a single core, Ni and Co concentrations of a single iron are approximately equal to those of the first crystallization products of the parent core[68,78]; therefore, we used the Ni and Co concentration of an iron meteorite to acquire the bulk composition of its parent core. Fractional crystallization modelling was performed for each ungrouped iron. For NC and CC ungrouped irons, we used 11 wt% and 3.5 wt% S (mean bulk S content of the parent cores of NC and CC groups, respectively[13]). The bulk Co and Ni concentrations acquired by the modelling were the upper limit of the parent core. Concentrations of Fe were calculated using $C_\mathrm{Fe} = 100 - C_\mathrm{Ni} - C_\mathrm{Co} - C_\mathrm{S}$ (where C denotes the concentration of each element).

Data availability

The authors declare that the data supporting the findings of this study are available within the article and its Extended Data files.

References

1. Kruijer, T. S. et al. Protracted core formation and rapid accretion of protoplanets. *Science (1979)* **344**, 1150–1154 (2014).
2. Goldstein, J. I., Scott, E. R. D. & Chabot, N. L. Iron meteorites: crystallization, thermal history, parent bodies, and origin. *Chem. der Erde* **69**, 293–325 (2009).
3. Kruijer, T. S., Burkhardt, C., Budde, G. & Kleine, T. Age of Jupiter inferred from the distinct genetics and formation times of meteorites. *Proc. Natl Acad. Sci. USA* **114**, 6712–6716 (2017).
4. Spitzer, F., Burkhardt, C., Nimmo, F. & Kleine, T. Nucleosynthetic Pt isotope anomalies and the Hf-W chronology of core formation in inner and outer solar system planetesimals. *Earth Planet. Sci. Lett.* **576**, 117211 (2021).
5. Youdin, A. N. & Goodman, J. Streaming instabilities in protoplanetary disks. *Astrophys. J.* **620**, 459–469 (2005).
6. Cuzzi, J. N., Hogan, R. C. & Shariff, K. Toward planetesimals: dense chondrule clumps in the protoplanetary nebula. *Astrophys. J.* **687**, 1432–1447 (2008).
7. Lichtenberg, T., Drążkowska, J., Schönbächler, M., Golabek, G. J. & Hands, T. O. Bifurcation of planetary building blocks during Solar System formation. *Science (1979)* **371**, 365–370 (2021).
8. Drążkowska, J. & Dullemond, C. P. Planetesimal formation during protoplanetary disk buildup. *Astron. Astrophys.* **614**, A62 (2018).
9. Izidoro, A. et al. Planetesimal rings as the cause of the Solar System's planetary architecture. *Nat. Astron.* **6**, 357–366 (2021).
10. Morbidelli, A. et al. Contemporary formation of early Solar System planetesimals at two distinct radial locations. *Nat. Astron.* **6**, 72–79 (2021).
11. Dauphas, N. The isotopic nature of the Earth's accreting material through time. *Nature* **541**, 521–524 (2017).
12. Burkhardt, C. et al. Terrestrial planet formation from lost inner solar system material. *Sci. Adv.* **7**, 7601 (2021).
13. Hilton, C. D., Ash, R. D. & Walker, R. J. Chemical characteristics of iron meteorite parent bodies. *Geochim. Cosmochim. Acta* **318**, 112–125 (2022).
14. Rubin, A. E. Carbonaceous and noncarbonaceous iron meteorites: differences in chemical, physical, and collective properties. *Meteorit. Planet. Sci.* **53**, 2357–2371 (2018).

15. Grossman, L., Fedkin, A. V. & Simon, S. B. Formation of the first oxidized iron in the solar system. *Meteorit. Planet. Sci.* **47**, 2160–2169 (2012).
16. Brearley, A. J. in *Meteorites and the Early Solar System II* (eds Lauretta, D. S. & McSween Jr., H. Y.) 587–624 (Univ. Arizona Press, 2006).
17. Fedkin, A. V. & Grossman, L. Effects of dust enrichment on oxygen fugacity of cosmic gases. *Meteorit. Planet. Sci.* **51**, 843–850 (2016).
18. Campbell, A. J. & Humayun, M. Compositions of group IVB iron meteorites and their parent melt. *Geochim. Cosmochim. Acta* **69**, 4733–4744 (2005).
19. Zhang, B., Chabot, N. L. & Rubin, A. E. Compositions of carbonaceous-type asteroidal cores in the early solar system. *Sci. Adv.* **8**, 5781 (2022).
20. Chabot, N. L. & Zhang, B. A revised trapped melt model for iron meteorites applied to the IIIAB group. *Meteorit. Planet. Sci.* **57**, 200–227 (2022).
21. Rubin, A. E., Zhang, B. & Chabot, N. L. IVA iron meteorites as late-stage crystallization products affected by multiple collisional events. *Geochim. Cosmochim. Acta* **331**, 1–17 (2022).
22. Zhang, B. et al. Chemical study of group IIIF iron meteorites and the potentially related pallasites Zinder and Northwest Africa 1911. *Geochim. Cosmochim. Acta* **323**, 202–219 (2022).
23. Wood, B. J., Smythe, D. J. & Harrison, T. The condensation temperatures of the elements: a reappraisal. *Am. Mineral.* **104**, 844–856 (2019).
24. Steenstra, E. S., Knibbe, J. S., Rai, N. & van Westrenen, W. Constraints on core formation in Vesta from metal–silicate partitioning of siderophile elements. *Geochim. Cosmochim. Acta* **177**, 48–61 (2016).
25. Wasson, J. T. & Kallemeyn, G. W. Compositions of chondrites. *Philosophical Transactions of the Royal Society A: Mathematical. Phys. Eng. Sci.* **325**, 535–544 (1988).
26. Larimer, J. W. & Anders, E. Chemical fractionations in meteorites—III. Major element fractionations in chondrites. *Geochim. Cosmochim. Acta* **34**, 367–387 (1970).
27. Wasson, J. T. Vesta and extensively melted asteroids: why HED meteorites are probably not from Vesta. *Earth Planet. Sci. Lett.* **381**, 138–146 (2013).
28. Spitzer, F., Burkhardt, C., Budde, G., Kruijer, T. S. & Kleine, T. Isotopic evolution of the protoplanetary disk as recorded in Mo isotopes of iron meteorites. In *51st Lunar and Planetary Science Conference* (LPI, 2020).
29. Bonnand, P. & Halliday, A. N. Oxidized conditions in iron meteorite parent bodies. *Nat. Geosci.* **11**, 401–404 (2018).
30. Benedix, G. K., Lauretta, D. S. & Mccoy, T. J. Thermodynamic constraints on the formation conditions of winonaites and silicate-bearing IAB irons. *Geochim. Cosmochim. Acta* **69**, 5123–5131 (2005).
31. Righter, K. & Drake, M. J. Core formation in Earth's Moon, Mars, and Vesta. *Icarus* **124**, 513–529 (1996).
32. Steenstra, E. S. et al. The effect of melt composition on metal-silicate partitioning of siderophile elements and constraints on core formation in the angrite parent body. *Geochim. Cosmochim. Acta* **212**, 62–83 (2017).
33. Righter, K., Sutton, S. R., Danielson, L., Pando, K. & Newville, M. Redox variations in the inner solar system with new constraints from vanadium XANES in spinels. *Am. Mineral.* **101**, 1928–1942 (2016).
34. Goodrich, C. A., Sutton, S. R., Wirick, S. & Jercinovic, M. J. Chromium valences in ureilite olivine and implications for ureilite petrogenesis. *Geochim. Cosmochim. Acta* **122**, 280–305 (2013).
35. Hewins, R. H. & Ulmer, G. C. Intrinsic oxygen fugacities of diogenites and mesosiderite clasts. *Geochim. Cosmochim. Acta* **48**, 1555–1560 (1984).
36. Schrader, D. L. & Zega, T. J. Petrographic and compositional indicators of formation and alteration conditions from LL chondrite sulfides. *Geochim. Cosmochim. Acta* **264**, 165–179 (2019).
37. Righter, K. & Neff, K. E. Temperature and oxygen fugacity constraints on CK and R chondrites and implications for water and oxidation in the early solar system. *Polar Sci.* **1**, 25–44 (2007).
38. Mckeown, D. A., Buechele, A. C., Tappero, R., Mccoy, T. J. & Gardner-Vandy, K. G. X-ray absorption characterization of Cr in forsterite within the MacAlpine Hills 88136 EL3 chondritic meteorite. *Am. Mineral.* **99**, 190–197 (2014).
39. Steenstra, E. S. & van Westrenen, W. Geochemical constraints on core-mantle differentiation in Mercury and the aubrite parent body. *Icarus* **340**, 113621 (2020).
40. Fogel, R. A. Aubrite basalt vitrophyres: the missing basaltic component and high-sulfur silicate melts. *Geochim. Cosmochim. Acta* **69**, 1633–1648 (2005).
41. Weisberg, M. K. & Kimura, M. The unequilibrated enstatite chondrites. *Chem. der Erde* **72**, 101–115 (2012).
42. Keil, K. Enstatite achondrite meteorites (aubrites) and the histories of their asteroidal parent bodies. *Geochemistry* **70**, 295–317 (2010).
43. Wai, C. M. & Wasson, J. T. Silicon concentrations in the metal of iron meteorites. *Geochim. Cosmochim. Acta* **33**, 1465–1471 (1969).
44. Pack, A., Vogel, I., Rollion-Bard, C., Luais, B. & Palme, H. Silicon in iron meteorite metal. *Meteorit. Planet. Sci.* **46**, 1470–1483 (2011).
45. Sugiura, N. & Fujiya, W. Correlated accretion ages and ε 54 Cr of meteorite parent bodies and the evolution of the solar nebula. *Meteorit. Planet. Sci.* **49**, 772–787 (2014).
46. Grossman, L. Condensation in the primitive solar nebula. *Geochim. Cosmochim. Acta* **36**, 597–619 (1972).
47. Grossman, L., Beckett, J. R., Fedkin, A. V., Simon, S. B. & Ciesla, F. J. Redox conditions in the solar nebula: observational, experimental, and theoretical constraints. *Rev. Mineral. Geochem.* **68**, 93–140 (2008).
48. Jones, R. H. Petrology and mineralogy of Type II, FeO-rich chondrules in Semarkona (LL3.0): origin by closed-system fractional crystallization, with evidence for supercooling. *Geochim. Cosmochim. Acta* **54**, 1785–1802 (1990).
49. Rubin, A. E., Dunn, T. L., Garner, K., Cecchi, M. & Hernandez, M. Barred olivine chondrules in ordinary chondrites: constraints on chondrule formation. *Meteorit. Planet. Sci.* https://doi.org/10.1111/MAPS.14046 (2023).
50. Schneider, J. M., Burkhardt, C., Marrocchi, Y., Brennecka, G. A. & Kleine, T. Early evolution of the solar accretion disk inferred from Cr-Ti-O isotopes in individual chondrules. *Earth Planet. Sci. Lett.* **551**, 116585 (2020).
51. Palme, H. & Boynton, W. V. in *Protostars and Planets III* (eds Levy, E. H. & Lunine, J. I.) 979–1004 (Univ. Arizona Press, 1993).
52. Ebel, D. S. & Grossman, L. Condensation in dust-enriched systems. *Geochim. Cosmochim. Acta* **64**, 339–366 (2000).
53. Sutton, S. et al. The bulk valence state of Fe and the origin of water in chondrites. *Geochim. Cosmochim. Acta* **211**, 115–132 (2017).
54. Le Guillou, C., Bernard, S., Brearley, A. J. & Remusat, L. Evolution of organic matter in Orgueil, Murchison and Renazzo during parent body aqueous alteration: In situ investigations. *Geochim. Cosmochim. Acta* **131**, 368–392 (2014).
55. Alexander, C. M. O., McKeegan, K. D. & Altwegg, K. Water reservoirs in small planetary bodies: meteorites, asteroids, and comets. *Space Sci. Rev.* **214**, 36 (2018).

56. Newcombe, M. E. et al. Degassing of early-formed planetesimals restricted water delivery to Earth. *Nature* **615**, 854–857 (2023).
57. Vorobyov, E. I. Variable accretion in the embedded phase of star formation. *Astrophys. J.* **704**, 715–723 (2009).
58. Jørgensen, J. K., Visser, R., Williams, J. P. & Bergin, E. A. Molecule sublimation as a tracer of protostellar accretion: evidence for accretion bursts from high angular resolution C18O images. *Astron. Astrophys.* **579**, A23 (2015).
59. Ciesla, F. & Lauretta, D. Radial migration and dehydration of phyllosilicates in the solar nebula. *Earth Planet. Sci. Lett.* **231**, 1–8 (2005).
60. Dittrich, K., Klahr, H. & Johansen, A. Gravoturbulent planetesimal formation: the positive effect of long-lived zonal flows. *Astrophys. J.* **763**, 117 (2013).
61. Lichtenberg, T. et al. A water budget dichotomy of rocky protoplanets from 26Al-heating. *Nat. Astron.* **3**, 307–313 (2019).
62. Grewal, D. S., Seales, J. D. & Dasgupta, R. Internal or external magma oceans in the earliest protoplanets – Perspectives from nitrogen and carbon fractionation. *Earth Planet. Sci. Lett.* **598**, 117847 (2022).
63. Grewal, D. S. & Asimow, P. D. Origin of the superchondritic carbon/nitrogen ratio of the bulk silicate Earth – an outlook from iron meteorites. *Geochim. Cosmochim. Acta* **344**, 146–159 (2023).
64. Grewal, D. S., Dasgupta, R. & Marty, B. A very early origin of isotopically distinct nitrogen in inner Solar System protoplanets. *Nat. Astron.* **5**, 356–364 (2021).
65. Hirschmann, M. M., Bergin, E. A., Blake, G. A., Ciesla, F. J. & Li, J. Early volatile depletion on planetesimals inferred from C–S systematics of iron meteorite parent bodies. *Proc. Natl Acad. Sci. USA* **118**, e2026779118 (2021).
66. Grewal, D. S. Origin of nitrogen isotopic variations in the rocky bodies of the Solar System. *Astrophys. J.* **937**, 123 (2022).
67. Grewal, D. S. et al. Limited nitrogen isotopic fractionation during core-mantle differentiation in rocky protoplanets and planets. *Geochim. Cosmochim. Acta* **338**, 347–364 (2022).
68. Chabot, N. L. Sulfur contents of the parental metallic cores of magmatic iron meteorites. *Geochim. Cosmochim. Acta* **68**, 3607–3618 (2004).
69. Schrader, D. L. et al. Distribution of 26Al in the CR chondrite chondrule-forming region of the protoplanetary disk. *Geochim. Cosmochim. Acta* **201**, 275–302 (2017).
70. Nie, N. X. et al. Meteorites have inherited nucleosynthetic anomalies of potassium-40 produced in supernovae. *Science (1979)* **379**, 372–376 (2023).
71. Tornabene, H. A., Ash, R. D., Walker, R. J. & Bermingham, K. R. Genetics, age, and crystallization history of group IC iron meteorites. *Geochim. Cosmochim. Acta* **340**, 108–119 (2023).
72. Wasson, J. T., Huber, H. & Malvin, D. J. Formation of IIAB iron meteorites. *Geochim. Cosmochim. Acta* **71**, 760–781 (2007).
73. Malvin, D. J., Wang, D. & Wasson, J. T. Chemical classification of iron meteorites—X. Multielement studies of 43 irons, resolution of group IIIE from IIIAB, and evaluation of Cu as a taxonomic parameter. *Geochim. Cosmochim. Acta* **48**, 785–804 (1984).
74. Buchwald, V. F. *Handbook of Iron Meteorites: Their History, Distribution, Composition and Structure* (Univ. California Press, 1975).
75. Jones, J. H. & Malvin, D. J. A nonmetal interaction model for the segregation of trace metals during solidification of Fe-Ni-S, Fe-Ni-P, and Fe-Ni-S-P alloys. *Metall. Trans. B* **21**, 697–706 (1990).
76. Wasson, J. T. Trapped melt in IIIAB irons; solid/liquid elemental partitioning during the fractionation of the IIIAB magma. *Geochim. Cosmochim. Acta* **63**, 2875–2889 (1999).
77. Wasson, J. T. Relationship between iron-meteorite composition and size: compositional distribution of irons from North Africa. *Geochim. Cosmochim. Acta* **75**, 1757–1772 (2011).
78. Chabot, N. L., Wollack, E. A., McDonough, W. F., Ash, R. D. & Saslow, S. A. Experimental determination of partitioning in the Fe-Ni system for applications to modeling meteoritic metals. *Meteorit. Planet. Sci.* **52**, 1133–1145 (2017).
79. Righter, K. & Drake, M. J. A magma ocean on Vesta: core formation and petrogenesis of eucrites and diogenites. *Meteorit. Planet. Sci.* **32**, 929–944 (1997).
80. Namur, O., Charlier, B., Holtz, F., Cartier, C. & McCammon, C. Sulfur solubility in reduced mafic silicate melts: implications for the speciation and distribution of sulfur on Mercury. *Earth Planet. Sci. Lett.* **448**, 102–114 (2016).
81. Rai, N. & Van Westrenen, W. Lunar core formation: new constraints from metal-silicate partitioning of siderophile elements. *Earth Planet. Sci. Lett.* **388**, 343–352 (2014).
82. Hirschmann, M. M. Magma oceans, iron and chromium redox, and the origin of comparatively oxidized planetary mantles. *Geochim. Cosmochim. Acta* **328**, 221–241 (2022).

Acknowledgements

We thank A. P. Vyas for helping to improve the clarity of our communication and we thank C. M. O'D. Alexander, G. Blake, K. Batygin and Y. Miyazaki for fruitful discussions during early stages of the research presented in this study. This study was funded by a Barr Foundation postdoctoral fellowship by Caltech awarded to D.S.G. B.Z. was supported by NASA grants 80NSSC19K1238 and 80NSSC23K0035.

Author contributions

D.S.G. conceived the project. D.S.G. compiled the data and performed the numerical calculations along with N.X.N. B.Z. performed the fractional crystallization calculations. A.I. helped with the astrophysical implications. All authors interpreted the data. D.S.G. wrote the manuscript with inputs from N.X.N., B.Z., A.I. and P.D.A.

Competing interests

The authors declare no competing interests.

Additional information

Extended data is available for this paper at https://doi.org/10.1038/s41550-023-02172-w.

Supplementary information The online version contains supplementary material available at https://doi.org/10.1038/s41550-023-02172-w.

Correspondence and requests for materials should be addressed to Damanveer S. Grewal.

Peer review information *Nature Astronomy* thanks Emily Worsham and the other, anonymous, reviewer(s) for their contribution to the peer review of this work.

Reprints and permissions information is available at www.nature.com/reprints.

Publisher's note Springer Nature remains neutral with regard to jurisdictional claims in published maps and institutional affiliations.

Springer Nature or its licensor (e.g. a society or other partner) holds exclusive rights to this article under a publishing agreement with the author(s) or other rightsholder(s); author self-archiving of the accepted manuscript version of this article is solely governed by the terms of such publishing agreement and applicable law.

© The Author(s), under exclusive licence to Springer Nature Limited 2024

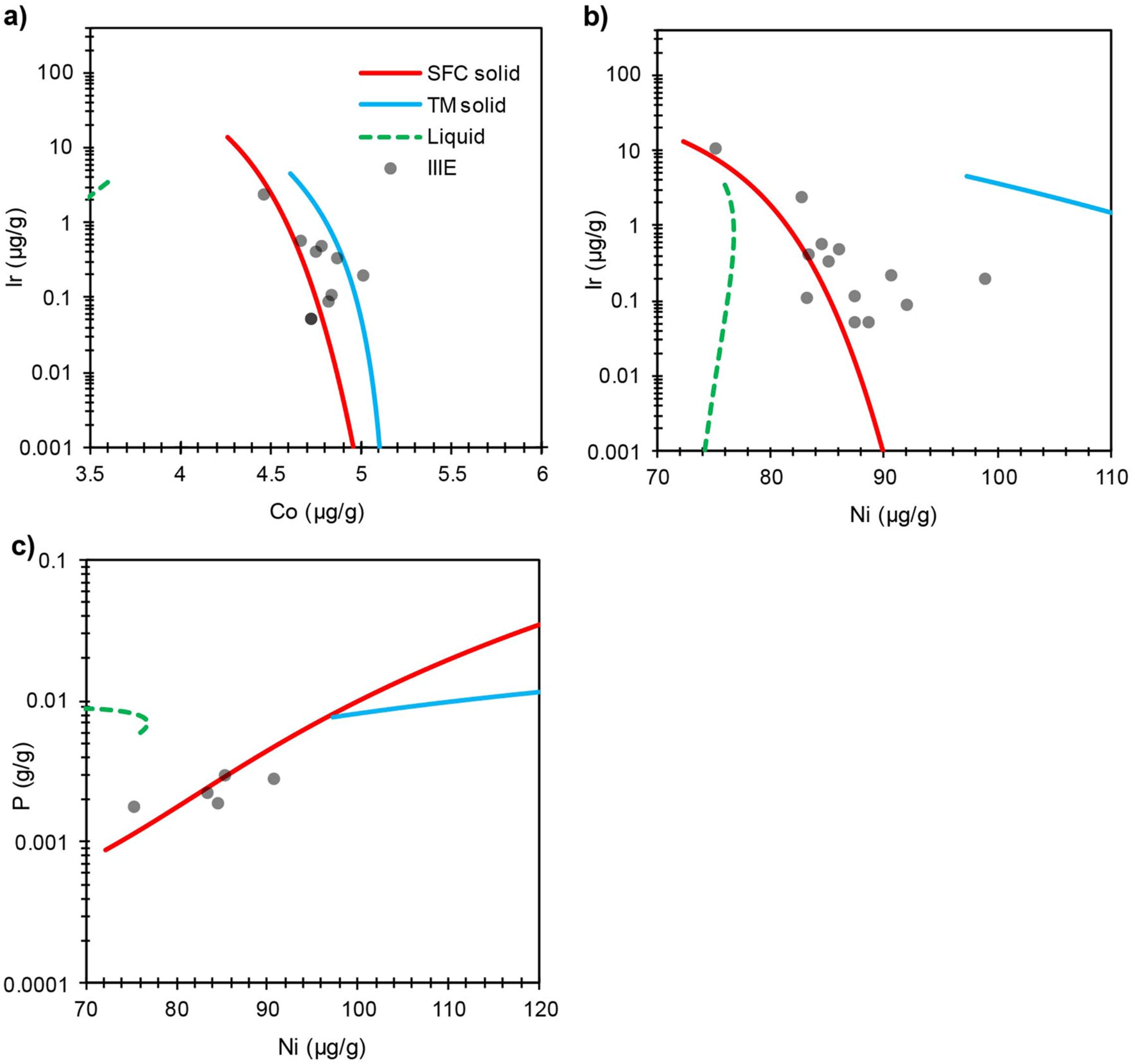

Extended Data Fig. 1 | Fractional crystallization modeling of P, Ni, Co, and Ir for group IIIE. The Ir-Co (**a**), Ir-Ni (**b**), and P-Ni (**c**) models use bulk 8 wt.% S and 0.6 wt.% P. The red lines, blue lines, and green dashed lines denote solid from simple fractional crystallization (SFC solid), solid from trapped melt (TM solid), and liquid (Liquid), respectively. Ir, Co, and Ni data are from ref. 73. Phosphorus data are from ref. 74.

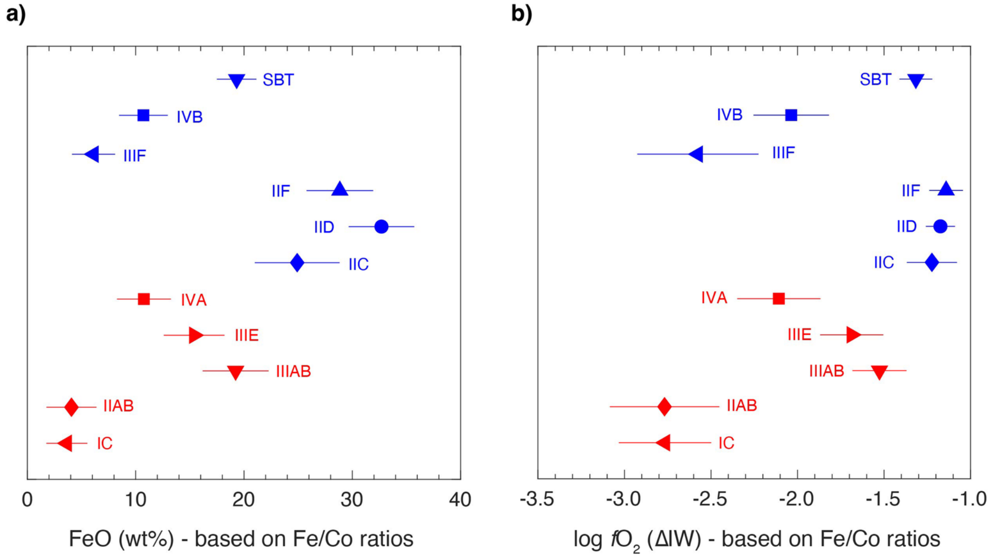

Extended Data Fig. 2 | Comparison between the FeO contents and fO_2 of IMPBs based on the Fe/Co ratios of their parent cores. In agreement with the calculations based on Fe/Ni ratios (Fig. 2), the estimated FeO contents (**a**) and fO_2 (**b**) of CC IMPBs (blue) based on Fe/Co ratios are either similar to or only modestly higher than those of NC IMPBs (red). Error bars for FeO content and fO_2 represent 1σ deviation obtained by the propagation of standard deviation of individual terms in Eqs. 1 and 2, respectively (for details refer to the caption of Fig. 2).

https://doi.org/10.1038/s41550-023-02172-w

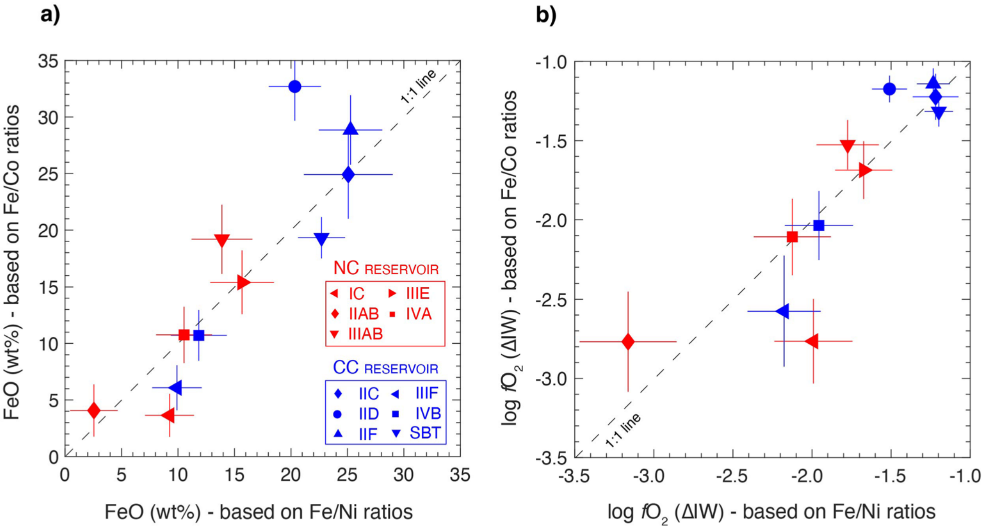

Extended Data Fig. 3 | Comparison between the FeO contents and fO_2 of IMPBs based on the Fe/Ni and Fe/Co ratios of their parent cores. The FeO contents (**a**) and fO_2 (**b**) of each NC and CC IMPB, except for groups IC and IID, estimated via Fe/Ni and Fe/Co ratios of their parent cores broadly agree with each other.

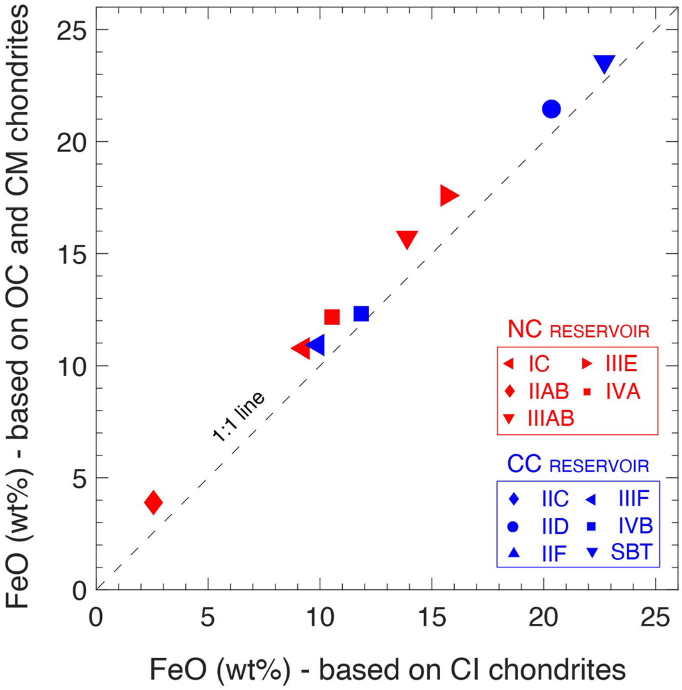

Extended Data Fig. 4 | Comparison between the mean FeO contents of the IMPBs based on the Fe/Ni ratios of CI and ordinary/CM chondrites. The FeO contents of IMPBs estimated using Fe/Ni ratios of ordinary and CM chondrites (for NC and CC IMPBs, respectively) and CI chondrites are approximately similar.

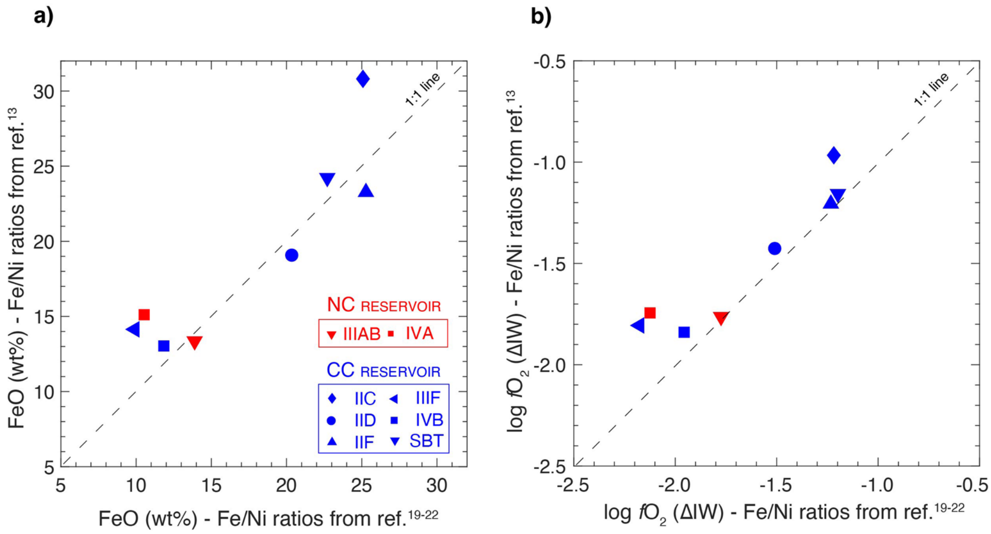

Extended Data Fig. 5 | Comparison between the FeO contents and fO_2 of the IMPBs based on the Fe/Ni ratios determined by different fractional crystallization models. The FeO content (**a**) and fO_2 (**b**) of each NC and CC IMPB, as determined by several fractional crystallization models, broadly agree with each other. The X-axis represents FeO contents and fO_2 values determined using the results from ref. 19–22, while the Y-axis represents values from ref. 13. Note that the data plotted on the X-axis are used for the discussion in this study. Data for group IC and group IIAB were not plotted since the compositions of their parent cores have only been determined in ref. 13. Additionally, data for group IIIE was not plotted as the composition of its parent core was determined only in this study.

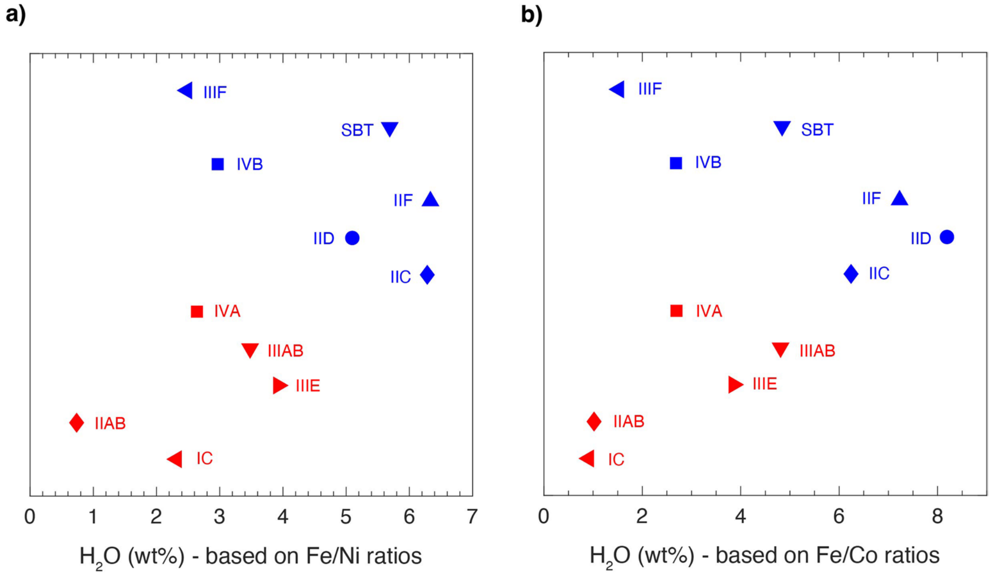

Extended Data Fig. 6 | Minimum water required to explain the FeO contents of the parent bodies of iron meteorites based on the Fe/Ni and Fe/Co ratios of their parent cores. Although CC IMPBs generally require higher water contents than NC IMPBs to explain their FeO contents (**a**, **b**), the amount of water accreted to explain the FeO contents of NC IMPBs is also substantial.

Extended Data Table 1 | Chemical compositions of the parent cores of NC and CC magmatic iron meteorites

Groups	**Fe (wt%)**	**Ni (wt%)**	**Co (wt%)**	**S (wt%)**	**P (wt%)**
		Magmatic NC Irons			
IC	75.0	6.0	0.2	19.0	0.1
IIAB	78.0	5.0	0.3	17.0	0.7
IIIAB	83.0	7.3	0.4	9.0	0.2
IIIE	83.4	7.6	0.4	8.0	0.6
IVA	89.3	7.3	0.4	3.0	0.1
		Magmatic CC Irons			
IIC	81.3	10.0	0.5	6.0	3.0
IID	86.6	10.8	0.7	0.0	1.0
IIF	81.7	11.9	0.6	5.0	0.4
IIIF	89.1	7.3	0.3	2.0	1.0
IVB	81.0	17.8	0.8	0.0	0.7
SBT	71.7	18.0	0.8	8.0	1.0

Data sources: Fe, Ni, S, and P contents of groups IC and IIAB – ref. 13; Co content of groups IC and IIAB – This study; Composition of group IIIAB – ref. 20, IIIE – This study; IVA – ref. 21; IIC, IID, IIF, IVB, and SBT – ref. 19; IIIF – ref. 22.

Extended Data Table 2 | FeO contents, fO_2, and minimum water contents of the parent bodies of NC and CC magmatic iron meteorites based on Fe/Ni and Fe/Co ratios of their parent cores

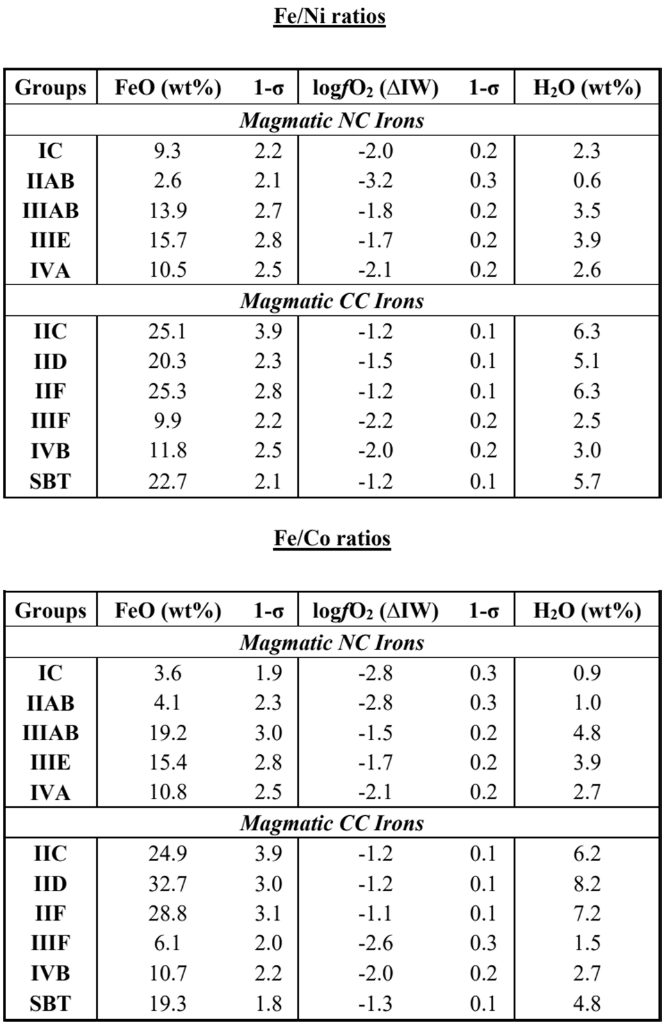

Fe/Ni ratios

Groups	FeO (wt%)	1-σ	$\log fO_2$ (ΔIW)	1-σ	H_2O (wt%)
			Magmatic NC Irons		
IC	9.3	2.2	-2.0	0.2	2.3
IIAB	2.6	2.1	-3.2	0.3	0.6
IIIAB	13.9	2.7	-1.8	0.2	3.5
IIIE	15.7	2.8	-1.7	0.2	3.9
IVA	10.5	2.5	-2.1	0.2	2.6
			Magmatic CC Irons		
IIC	25.1	3.9	-1.2	0.1	6.3
IID	20.3	2.3	-1.5	0.1	5.1
IIF	25.3	2.8	-1.2	0.1	6.3
IIIF	9.9	2.2	-2.2	0.2	2.5
IVB	11.8	2.5	-2.0	0.2	3.0
SBT	22.7	2.1	-1.2	0.1	5.7

Fe/Co ratios

Groups	FeO (wt%)	1-σ	$\log fO_2$ (ΔIW)	1-σ	H_2O (wt%)
			Magmatic NC Irons		
IC	3.6	1.9	-2.8	0.3	0.9
IIAB	4.1	2.3	-2.8	0.3	1.0
IIIAB	19.2	3.0	-1.5	0.2	4.8
IIIE	15.4	2.8	-1.7	0.2	3.9
IVA	10.8	2.5	-2.1	0.2	2.7
			Magmatic CC Irons		
IIC	24.9	3.9	-1.2	0.1	6.2
IID	32.7	3.0	-1.2	0.1	8.2
IIF	28.8	3.1	-1.1	0.1	7.2
IIIF	6.1	2.0	-2.6	0.3	1.5
IVB	10.7	2.2	-2.0	0.2	2.7
SBT	19.3	1.8	-1.3	0.1	4.8

For details related to the calculated values, refer to the main text.

Extended Data Table 3 | Fe, Ni, Co, and S contents of the parent cores, and FeO contents and fO_2 of the parent bodies of ungrouped magmatic iron meteorites from the NC and CC reservoirs

					Fe/Ni		*Fe/Co*	
Groups	**Fe (wt.%)**	**Ni (wt.%)**	**Co (wt.%)**	**S (wt.%)**	**FeO (wt%)**	**logfO_2 (ΔIW)**	**FeO (wt%)**	**logfO_2 (ΔIW)**
Ungrouped Magmatic NC Irons								
Cambria	78.3	10.3	0.4	11.0	32.9	-0.9	25.7	-1.1
Reed City	80.7	7.9	0.5	11.0	18.2	-1.5	31.0	-1.1
Ungrouped Magmatic CC Irons								
Grand Rapids	85.7	10.3	0.5	3.5	17.0	-1.7	19.9	-1.5
La Caille	85.6	10.3	0.6	3.5	17.3	-1.6	23.3	-1.4
Mbosi	86.1	9.7	0.8	3.5	15.0	-1.8	36.3	-1.1
New Baltimore	89.0	6.9	0.6	3.5	5.4	-2.7	22.0	-1.6

For details related to the calculated values, refer to the main text and methods section.

Extended Data Table 4 | Oxidation states of rocky bodies in the solar system

Rocky bodies	logfO_2 (ΔIW)	1-σ	Methodology	Reference
Carbonaceous chondrites	0 to 2	-	Mineral equilibria	Ref.[33]
IVB	-1.0	-	Assuming a refractory-enriched chondritic silicate composition	Ref.[18]
IVA	-1.0	0.2	Cr conc. in irons	Ref.[29]
IAB-MG, ung	-2.8	0.4	Quartz-Iron-Ferrosilite reaction	Ref.[30]
IAB-MG, ung	-1.8	-	Coexisting metal, opx and olivine	Ref.[79]
IIE	-1.5	0.2	Coexisting metal, opx and olivine	Ref.[79]
Vesta	-2.2	0.2	Core-mantle differentiation	Ref.[24]
Angrite parent body	-1.4	0.5	Core-mantle differentiation	Ref.[32]
Acapulcoites	-2.0	0.2	Coexisting metal, opx and olivine	Ref.[79]
Winonaites	-2.7	0.2	Quartz-Iron-Ferrosilite reaction	Ref.[30]
Brachinites	-0.1	0.5	V-pre-edge peak in spinels	Ref.[33]
Ureilites	-2.4	0.6	Cr valency in olivine cores	Ref.[34]
Pallasites	-0.5	0.6	V-pre-edge peak in spinels	Ref.[33]
Lodranites	-2.0	1.1	V-pre-edge peak in spinels	Ref.[33]
Mesosiderites	0.0	0.5	Electrochemical Measurements	Ref.[35]
H	-1.5	-	Coexisting metal, opx and olivine	Ref.[79]
L	-1.4	0.1	Coexisting metal, opx and olivine	Ref.[79]
LL	-1.4	0.1	Coexisting metal, opx and olivine	Ref.[79]
RC	1.0	1.0	Mineral equilibria	Ref.[37]
EL3	-7.3	0.8	Cr valency in olivine	Ref.[38]
Aubrite parent body	-6.0	0.5	Basaltic vitrophyres in aubrites	Ref.[39]
CAIs	-7.8	-	Ti valency in fassaite	Ref.[47]
Mercury	-5.4	0.4	Core-mantle differentiation	Ref.[80]
Moon	-1.9	0.2	Core-mantle differentiation	Ref.[81]
Mars	-1.4	0.2	Core-mantle differentiation	Ref.[82]
Earth	-2.0	0.6	Final core-mantle differentiation event	Ref.[82]

Note that the fO_2 values were reported using an ideal solution model ($\gamma_{\mathrm{Fe}}^{\mathrm{metal}}$ and $\gamma_{\mathrm{FeO}}^{\mathrm{silicate}} = 1$).